ADVANCED OPTICAL MATERIALS
www.advopticalmat.de

Simultaneous Conversion of Polarization and Frequency via Time-Division-Multiplexing Metasurfaces

Jin Yang, Jun Chen Ke, Wen Kang Cao, Ming Zheng Chen, Qiang Cheng, Vincenzo Galdi,* and Tie Jun Cui**

Metasurfaces are artificially engineered two-dimensional materials composed of sub-wavelength meta-atoms, which have shown unprecedented capabilities in manipulating the amplitude, phase, frequency, and polarization states of electromagnetic waves. Specifically, polarization control can be attained via suitable anisotropic, linear, and time-invariant designs, while frequency conversion is realized via nonlinear or time-varying platforms. Simultaneous manipulations of polarization and frequency would be of considerable practical interest in many application scenarios, but remain unattainable with current approaches. Here, a time-division-multiplexing metasurface is proposed to realize the simultaneous conversion of polarization and frequency. The platform relies on time-modulated polarization switches and, by varying the duty cycle and time delays of the polarization channels, can arbitrarily rotate the polarization at the central frequency of operation, and synthesize various polarization states at selected harmonic frequencies. Theoretical predictions are validated via measurements on a prototype operating at microwave frequencies, providing the first experimental evidence of simultaneous polarization and frequency conversions via time-division-multiplexing metasurfaces. The outcomes open a new pathway in manipulating the electromagnetic waves via time-varying metasurfaces, and may be of interest for a broad variety of applications in scenarios ranging from polarization imaging to quantum optics.

1. Introduction

Polarization is a fundamental property of electromagnetic (EM) waves,and its manipulation is crucial in many applications, ranging from radio-frequency to optical scenarios.[1–8] To realize polarization control, various types of converters have been designed at microwave and terahertz frequencies,[9,10] whereas dielectric metasurfaces and meta-gratings[5,11–13] have been proposed at optical wavelengths. Specifically, metasurfaces featuring spatial arrangements of anisotropic sub-wavelength elements enable precise polarization control by imparting independent and arbitrary phase profiles on two orthogonal linearly polarized wavefronts.[14–18] Alternative configurations exploit the geometric (or Pancharatnam-Berry) phase,[19–22] which can induce opposite phase profiles on two orthogonal circularly polarized components.

Typical metasurface-based configurations exhibit *static* polarization responses once the geometrical parameters are fixed, whereas *dynamic* control is highly desirable in many practical applications. Programmable or tunable metasurfaces[23,24] incorporating active elements (e.g., diodes, graphene, phase-change materials) can be exploited to this aim. For instance, anisotropic reflective metasurfaces[14] based on voltage-controlled varactors have been demonstrated to realize independent dual-polarization wavefront control, and transmission-type metasurfaces with dynamically tunable properties[25] have been shown to rotate the incident-wave polarization without altering its axial ratio. However, these designs provide limited tunability, and still operate in a linear and time-invariant regime. This prevents the simultaneous conversion of polarization and frequency, which could be of great interest in many practical applications.

At visible wavelengths, non-reciprocal plasmonic thin films based on the Faraday rotation effect[26] have been proven to realize tunable and switchable polarization rotation, although their maximum tuning angle (≈8.4°) is still insufficient for most practical applications. To overcome this limitation, strongly anisotropic nonlinear metamaterials[27] have been exploited to realize all-optical switching of visible-light polarization, attaining up to ≈60° rotation of the polarization ellipse at

J. Yang, J. C. Ke, W. K. Cao, M. Z. Chen, Q. Cheng, T. J. Cui
State Key Laboratory of Millimeter Waves
Southeast University
Nanjing 210096, China
E-mail: qiangcheng@seu.edu.cn; tjcui@seu.edu.cn
V. Galdi
Fields & Waves Lab
Department of Engineering
University of Sannio
Benevento I-82100, Italy
E-mail: vgaldi@unisannio.it
The ORCID identification number(s) for the author(s) of this article can be found under https://doi.org/10.1002/adom.202101043.

DOI: 10.1002/adom.202101043

picosecond timescales. Conversely, at microwave frequencies, there is a lack of systematic research on nonlinear schemes for polarization control. Recently, space-time coding digital metasurfaces[28–35] have been put forward to manipulate EM waves simultaneously in both the space and frequency domains. By assuming meta-atoms with time-varying (phase or amplitude) reflection responses,[28] these metasurfaces can effectively manipulate the frequency spectrum of the reflected field, resulting in the generation of harmonic waves, whose properties can be controlled in a flexible and precise fashion.[29–34] This provides a suitable platform to realize nonlinear polarization control for microwave fields.

Here, we put forward the concept of *time-division-multiplexing metasurface* (TDMM) to attain the simultaneous conversion of polarization and frequency. Specifically, we introduce a general theory for the independent control of two polarizations and the manipulation of the harmonic phases. We provide several numerical examples of various polarizations synthesized at the harmonic frequencies. For experimental validation, we fabricate and characterize a TDMM prototype loaded with positive-intrinsic-negative (PIN) diodes, demonstrating good agreement with the theoretical predictions.

Our results provide the first demonstration of simultaneous polarization and frequency conversions via a time-division-multiplexing approach, which opens up an entirely new direction in space-time metasurfaces for complex EM manipulations. The proposed approach can be exploited to realize high-speed polarization-division multiplexing transmission for both microwave and fiber optic communication systems. When combined with amplitude/phase modulation schemes, it can provide new degrees of freedom to realize complex EM functionalities, including multiplexed holography, adaptive beamforming, and cognitive radars.

2. Results and Discussion

Referring to **Figure 1** for conceptual illustration, our proposed TDMM comprises a two-dimensional (2-D) array of $M \times N$ elements loaded with active components (PIN diodes). Different from conventional schemes based on phase or amplitude modulation, the generic element acts as polarization switch, allowing the transmission of either *x*- or *y*-polarized fields, depending on the working states (on/off) of the diodes (Figure 1a). The diodes can be set and reconfigured across the array, both in space and time, by controlling the biasing voltages via a field-gate programmable array (FPGA). For instance, Figure 1b illustrates a *space-domain* approach, where the polarization states are fixed in time and varied across the elements. An anisotropic time-domain metasurface can control the harmonic polarizations by independently manipulating the harmonic phases of two orthogonally polarized waves.[32] However, the space-domain synthesis method suffers from critical drawbacks. First, varactor diodes are required to adjust the amplitude and phase responses continuously along the orthogonal directions, leading to high biasing voltages from external direct-current sources, which limits the switching speed and the operational bandwidth. Second, for the best performance, the incident polarization should be tilted at an angle of 45° with respect to the array axes, which curtails the range of applicability.

To overcome the above limitations, here we explore a different mechanism based on the *time-domain* switching of the polarization state, as illustrated in Figure 1c. This approach can work for arbitrarily incident polarizations, and relies on PIN diodes, which exhibit low biasing voltage and wide bandwidth. In what follows, we outline the basic theory which enables the simultaneous conversion of polarization and frequency. Specifically, we show that, by suitably designing the time-switching process, it is possible to rotate a linear polarization arbitrarily at

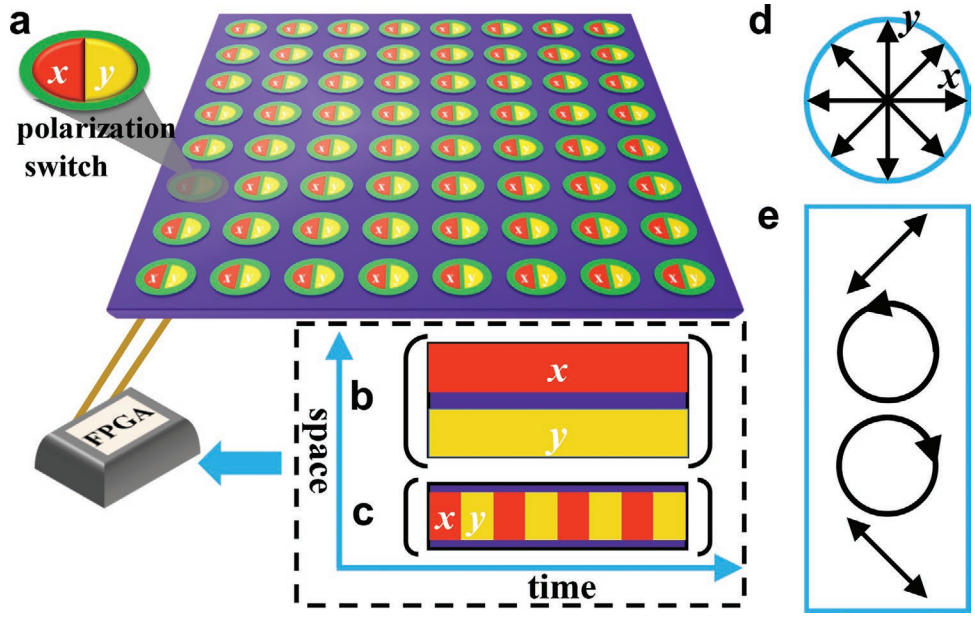

Figure 1. Conceptual illustration of TDMM. a) Schematic of a 2-D array of polarization switches controlled by FPGA. b,c) Space- and time-domain approaches, respectively. d) 180° rotation of linear polarization at the central operation frequency. e) Four basic polarization states synthesized at harmonic frequencies: ±45° linear polarizations, and two orthogonal circular polarizations.

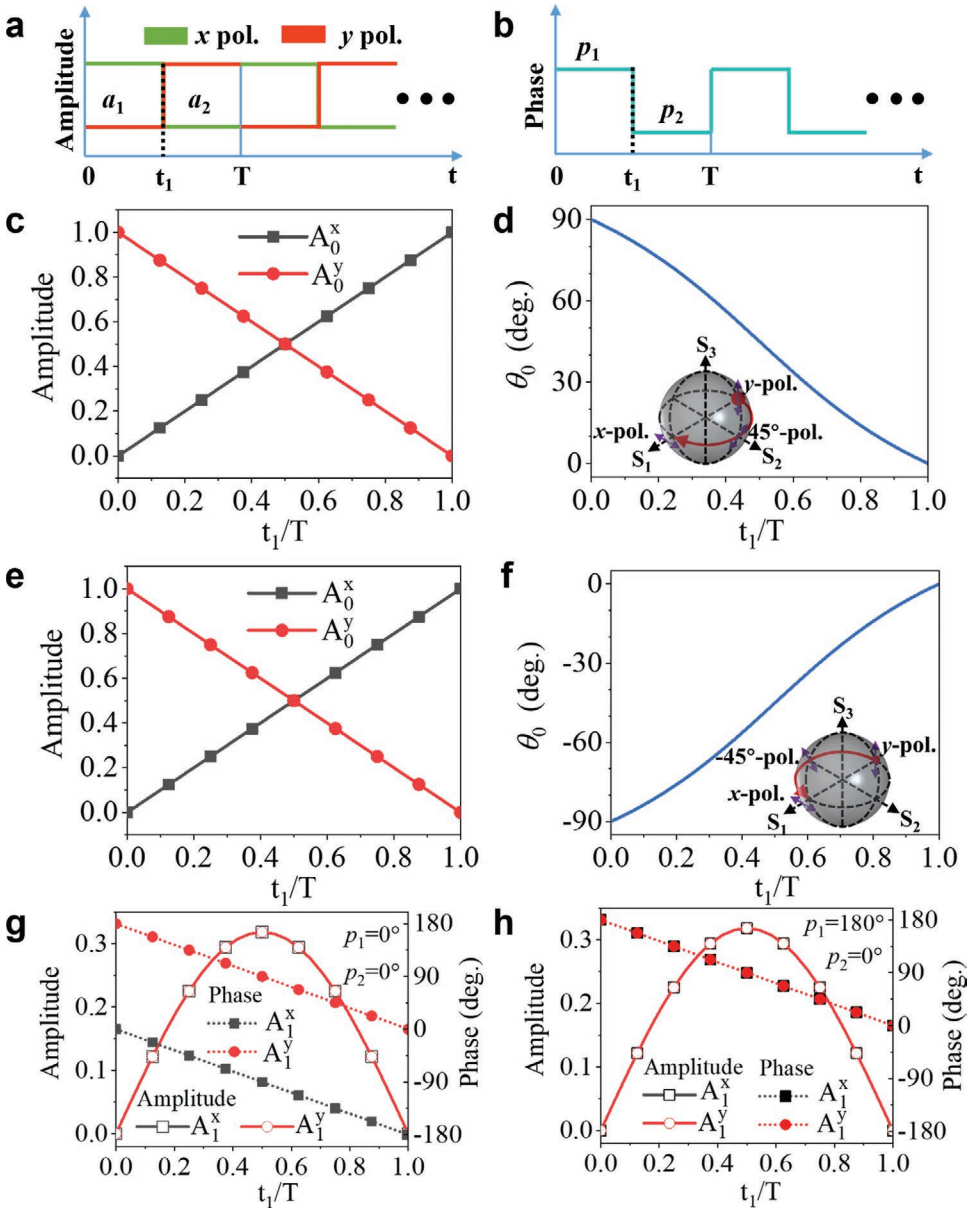

Figure 2. a,b) Periodic modulation of the transmitted amplitude and phase, respectively, for the two polarization channels. c,d) Calculated (real-valued) amplitudes for the *x*- and *y*-polarizations and corresponding tilt angle, respectively, for $p_1 = p_2 = 0°$, as a function of the duty cycle. e,f) Same as above, but for $p_1 = 180°$, $p_2 = 0°$. g,h) Calculated amplitudes and phases for the *x*- and *y*-polarizations at 1st harmonic order, as a function of duty cycle, for $p_1 = p_2 = 0°$ and $p_1 = 180^0$, $p_2 = 0°$ respectively. The insets show linearly polarized states on the Poincaré sphere.

the central frequency (Figure 1d), and realize various polarization states at the harmonic frequencies (Figure 1e).

As schematized in **Figure 2**a,b, for each element, we assume a time-varying and periodic transmission function with period T and modulation frequency $f_0 = 1/T$. In each period, the *x*-polarization is transmitted with phase p_1 within the interval $0 \le t < t_1$, whereas the *y*-polarization is transmitted with phase p_2 within the interval $t_1 \le t < T$. Accordingly, for a suppressed $e^{j2\pi f_c t_c}$ time-harmonic dependence, the transmission function within a period can be defined as:

$$\tau(t) = \begin{cases} a_1 e^{jp_1}, & 0 \le t < t_1 \\ a_2 e^{jp_2}, & t_1 \le t < T \end{cases} \tag{1}$$

with a_1 and a_2 denoting some polarization-dependent amplitude factors, namely, $a_1 = a_x$ and $a_2 = 0$ for the *x*-polarization, and $a_1 = 0$ and $a_2 = a_y$ for the *y*-polarization. As an effect of the temporal modulation, the transmitted field will contain not only the central operational frequency f_c but also harmonic frequencies $f_c \pm kf_0$, with k integer. For modulation frequencies much smaller than the central operational frequency, i.e., $f_0 \ll f_c$, an adiabatic approximation can be applied,[29,30] and the complex amplitudes for the *x*- and *y*-polarizations at the generic k-th harmonic orders (A_k^x and A_k^y, respectively) can be computed explicitly by expanding in a Fourier series the transmission function (see the Supporting Information for details). In particular, for each

harmonic order, the polarization angle θ_k (tangent) can be expressed as:

$$\tan\Theta_k = \frac{A_k^y}{A_k^x} = \begin{cases} \frac{a_y}{a_x} e^{j(p_2-p_1)} \left(\frac{1-R_x}{R_x}\right), k=0 \\ -\frac{a_y}{a_x} e^{j(p_2-p_1)}, k\neq 0 \end{cases} \quad (2)$$

where $R_x = t_1/T$ denotes the duty cycle for the *x*-polarization.

From Equation (2), we observe that the polarization state at the central ($k = 0$) and harmonic ($k \neq 0$) frequencies can be altered by acting on the phase difference $\Delta p = p_2 - p_1$, amplitude factors a_x, a_y, and duty cycle R_x. In what follows, we illustrate some notable cases.

Assuming, for instance, $a_x = a_y$ and $p_2 = p_1$, Equation (2) can be rewritten as:

$$\tan\theta_k = \begin{cases} \frac{1-R_x}{R_x}, k=0 \\ -1, k\neq 0 \end{cases} \quad (3)$$

which implies a linear polarization, whose angle is fixed (–45°) at the harmonic frequencies ($k \neq 0$), whereas at the central frequency ($k = 0$) it can be varied within the interval [0°, 90°] by acting on the duty cycle R_x. Figure 2c shows the (real-valued) amplitudes A_0^x and A_0^y at the central frequency, as a function of the duty cycle, whereas Figure 2d shows the corresponding polarization angle θ_0. Figure 2g shows instead the complex-valued amplitudes pertaining to the first harmonic order ($k = 1$), from which we observe equal magnitudes and a phase difference of 180°, consistent with the polarization angle of –45° predicted by Equation (3).

Likewise, it follows from Equation (2) that, by assuming $a_x = a_y$ and $p_2 = p_1 + 180°$, a linear polarization is attained, with an angle tunable within the range [–90°,0°] at the central frequency (see Figure 2e,f), and fixed at 45° at the harmonic frequencies (see Figure 2h).

As previously mentioned, and apparent from Equation (2), varying the phase difference $\Delta p = p_2 - p_1$ would provide additional degrees of freedom for tailoring the polarization state at the harmonic frequencies. However, our PIN-diode-based architecture imposes some inherent limitations in finely tailoring this parameter. To overcome this problem, we introduce a more general time modulation in the periodic transmission function, viz.,

$$\tau(t) = \begin{cases} a_1 e^{j\varphi(t)}, 0 \le t < T/2 \\ a_2 e^{j\varphi(t)}, T/2 \le t < T \end{cases} \quad (4)$$

where $\varphi(t)$ is a time-varying phase (generally different for the two polarization channels). As detailed in the Supporting Information, this enables the independent control of the complex Fourier amplitudes for the *x*- and *y*-polarizations at the generic even-order ($k = 2m$) harmonic frequencies. Based on this observation, it is possible to establish a general synthesis strategy, schematically illustrated in **Figure 3**. The procedure entails two steps, as shown in Figure 3a–c. First, the time-varying phase signals $\varphi_x(t)$ (Figure 3a) and $\varphi_y(t)$ (Figure 3b) are synthesized independently in order to attain some desired Fourier amplitude and phase distributions (at even orders $k = 2m$) for the two polarizations (Figure 3d,e). Second, as illustrated in Figure 3c, these signals are *temporally intertwined* via the polarization switches, so that the individually synthesized spectral distributions for the two polarizations are effectively superposed. This enables the simultaneous and independent control of the polarization state at even-order ($k = 2m$) harmonic frequencies.

Within this framework, we note that the independent control of the phase response for the two polarizations is crucial, but challenging to attain. An additional degree of freedom can be created by recalling that introducing a time delay t_d in the time-varying transmission signal yields an additional phase shift $e^{-j2\pi k f_0 t_d}$ at the *k*-th order harmonic frequency. Accordingly, in the general scheme of Figure 3, we assume the same time-varying phase signal for both polarizations, but with different time delays,

$$\varphi_x(t) = \varphi(t - t_x), \varphi_y(t) = \varphi(t - t_y) \quad (5)$$

It can be shown (see the Supporting Information) that this still enables the independent control of the harmonic phase differences (at even orders $k = 2m$) for the two polarizations.

These effects are quantitatively illustrated in **Figure 4**. Specifically, Figure 4a,b shows the temporally intertwined signals featuring time delays t_x and t_y in *x*- and *y*-polarized channels, respectively. The corresponding harmonic intensity and phase distributions at the $k = \pm 2$ harmonic orders are shown in Figure 4c–f. As expected, the intensities do not depend on the time delays. Conversely, by varying the time delay t_x within the interval [0, $T/2$], a broad harmonic phase coverage of 360° with good phase linearity is attained for the *x*-polarization (Figure 4c,e), while maintaining the harmonic phase for the *y*-polarization unaffected. Clearly, due to the time shift property of the Fourier transform, the slope of the harmonic phase curve varies with the harmonic order. Similar results are observed for the *y*-polarization, by varying the time delay t_y (Figure 4d,f).

Based on the above results, the harmonic phase distributions for two orthogonal polarizations can be independently tailored by adjusting the time delays in the two polarization channels, thereby enabling the synthesis of desired polarization states via suitable temporal intertwining. Some representative examples of linear and circular polarizations are shown in the Supporting Information (see Figures S1 and S2, and Table S1, Supporting Information).

For a proof-of-concept demonstration of a TDMM, we consider the meta-atom in **Figure 5**a, comprising five metallic layers, two glue layers and two identical substrates. From top to bottom, the five metallic layers include: a receiving patch (Figure 5b), biasing lines for the receiving patch (Figure 5c), a ground plane, biasing lines for the transmitting patch (same as Figure 5c), and a transmitting patch (Figure 5d); the positive and negative diode electrodes are marked with the symbols "+" and "–", respectively. The geometry is described in more detail in the Supporting Information. Essentially, the receiving patch on the top layer is used to manipulate the transmission phase, while the transmitting patch on the bottom layer is used to control the polarization state of the transmitted wavefront. The PIN diodes D1 and D2 embedded in the receiving patch work in opposite

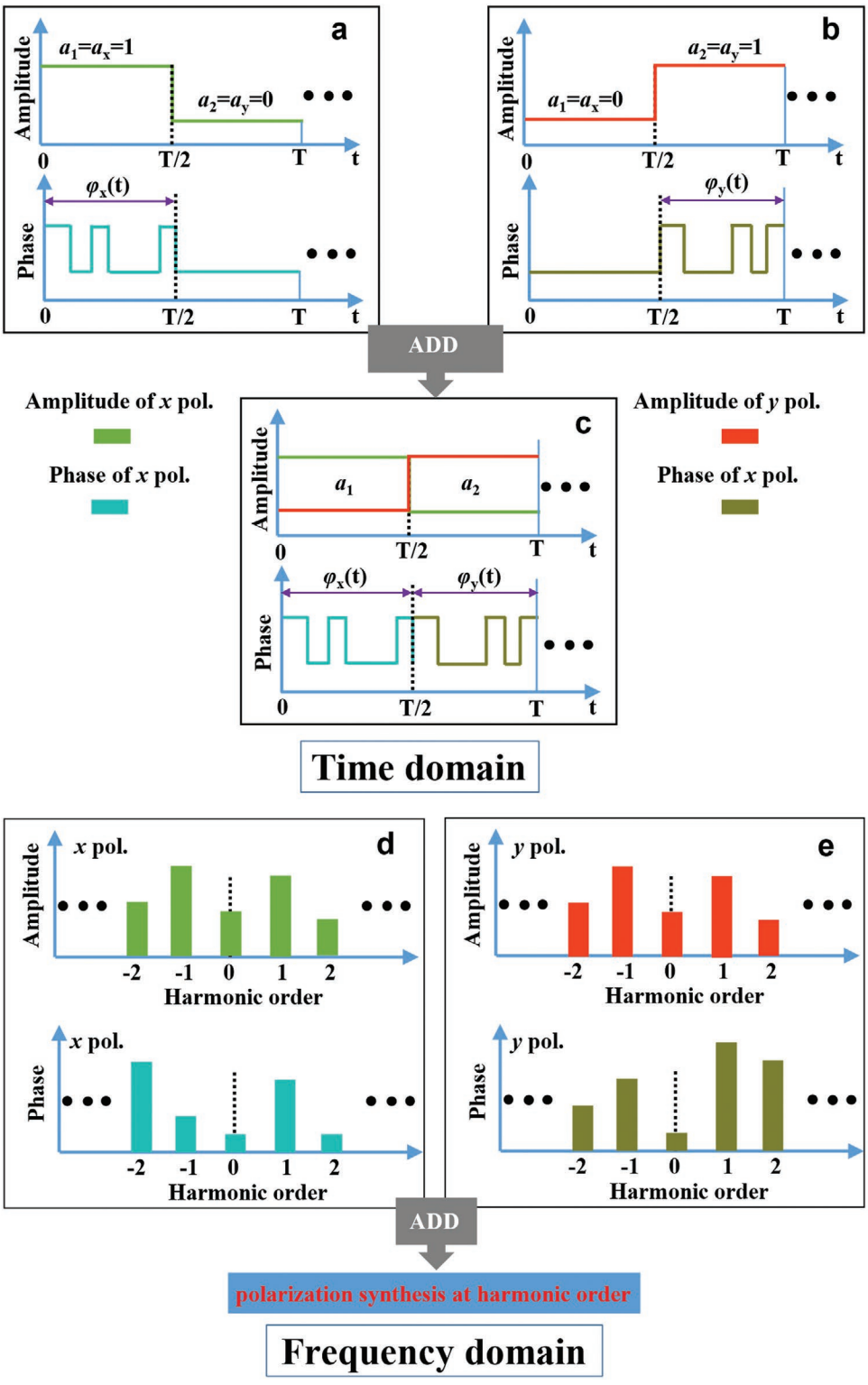

Figure 3. Schematic of polarization synthesis. a,b) Periodic modulation of transmitted amplitude and phase for the *x*- and *y*-polarization, respectively. c) Temporal intertwining of the two modulated polarizations. d,e) Corresponding harmonic intensity/phase distributions for the *x*- and *y*-polarizations, respectively.

states (one switched on, and the other off). By suitably switching their working states, a 180° phase difference can be generated based on the current reversal mechanism.[36] In the transmitting patch, when the PIN diodes D3 and D4 are switched on and off, respectively, a *y*-polarized wave is transmitted. By reversing the bias, an *x*-polarized wave is transmitted instead.

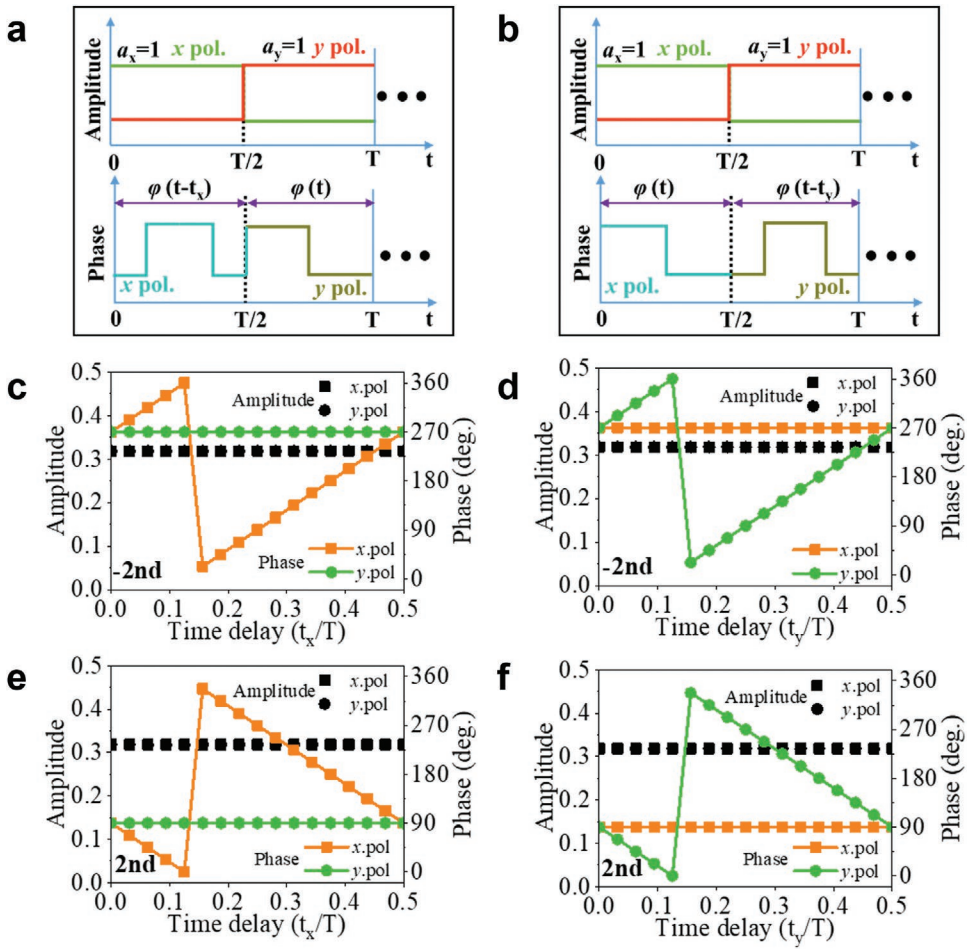

Figure 4. Effects of time delay. a,b) Temporal intertwining of the two modulated polarizations, assuming a time delay t_x for the *x*-polarization, and t_y for the *y*-polarization, respectively. c,d) Calculated amplitudes and phases for the *x*- and *y*-polarizations at –2nd harmonic order, as a function of time delays t_x and t_y, respectively. e,f) Same as above, but at 2nd harmonic order.

Full-wave numerical simulations of the designed meta-atom, detailed in the Supporting Information (see Figure S3, Supporting Information), confirm that the transmitted polarization and phase can be dynamically and independently controlled within the frequency range 10.5–11 GHz by suitably selecting the working states of the PIN diodes D1–D4. Accordingly, assuming a *y*-polarized incident field, we identify four possible transmission states: "T_{yy}/0°", "T_{yy}/180°", "T_{xy}/0°", and "T_{xy}/180°", corresponding to the combinations of co-polarized and cross-polarized, in-phase and out-of-phase transmission. These states can be associated with the coding digits "0/1", "0/0", "1/1", and "1/0", respectively, with the bits before and after the slash symbol (/) representing the polarization and phase, respectively, of the dominant transmitted component.

Based on the above design, a 17 × 17-element prototype is fabricated (with a total area of 214.2 × 214.2 mm^2), and measurements are carried out in a microwave chamber (see Figure S4, Supporting Information), with results summarized in **Figure 6**.

Specifically, Figure 6a–d shows the measured transmission responses (amplitudes and phases of T_{yy} and T_{xy}) within the frequency range 10–12 GHz, for *y*-polarized normal incidence and different combinations of the PIN diode states. As can be observed, the transmitted field is predominantly co-polarized when the PIN diodes D3 and D4 are in the on and off states, respectively; conversely, it is predominantly cross-polarized when the bias is reversed. By comparison with the simulated results (Figure S3, Supporting Information), the operation band shifts toward higher frequencies and a larger insertion loss is observed, due to the unavoidable design imperfections, modeling and measurement uncertainties, and fabrication tolerances. From the phase responses in Figure 6c,d, we observe that by switching the states of the PIN diodes D1 and D2, a phase difference of ≈180° is attained in both the co-polarized and cross-polarized transmitted fields, corresponding to the 1-bit coding phase states. For a proper behavior of the aforementioned four transmission states, the polarization isolation should be as high as possible, and the amplitudes of the dominant components should be equal and as large as possible. A good compromise among these conditions is observed at 11.28 GHz, where a polarization isolation above 9 dB is attained for both the co-polarized and cross-polarized responses, corresponding to the *y*- and *x*-polarized channels, respectively (see Table S2, Supporting Information).

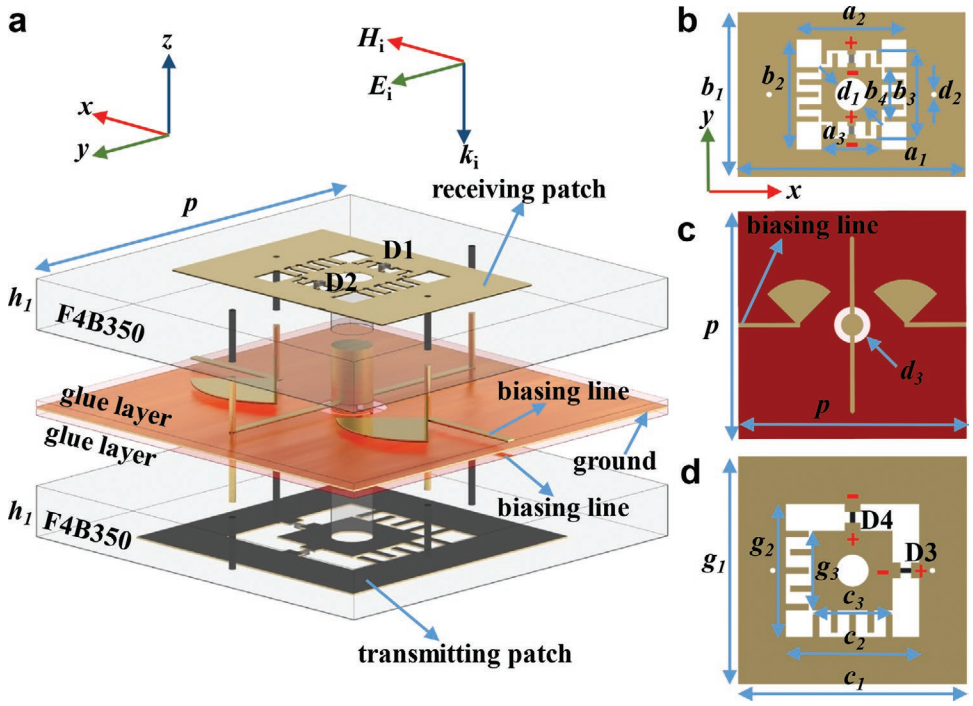

Figure 5. Designed meta-atom. a) 3-D geometry. b) Receiving patch with PIN diodes D1 and D2. c) Biasing layer. d) Transmitting patch with PIN diodes D3 and D4. The red symbols "+" and "–" identify the positive and negative diode electrodes, respectively. The dimensions (in mm) of the parameters are: $p = 12.6$, $h_1 = 1.5$, $a_1 = 8.3$, $a_2 = 4$, $a_3 = 2.2$, $b_1 = 6$, $b_2 = 4$, $b_3 = 3.2$, $b_4 = 2$, $d_1 = 1.2$, $d_3 = 2$, $c_1 = 8.6$, $c_2 = 5$, $c_3 = 3$, $g_1 = 8.6$, $g_2 = 5$, $g_3 = 3$.

There are two main factors responsible for the discrepancies between the simulated and measured results for the meta-atom. 1) Parameter uncertainties and unmodeled effects, including the parasitic effects the PIN diode (approximately modeled via an equivalent circuit valid around 11.28 GHz), fabrication tolerances, relative permittivity of substrate layers and glue layers, leakage effects around the gap between the sample and holder. 2) The simulated results are obtained by assuming plane-wave incidence and periodic boundary conditions, whereas, in the experiment, the incident wavefront is not strictly planar and the size of metasurface is limited. Nevertheless, a 180° phase difference, with good polarization isolation, high and equal amplitudes of the dominant components, can be obtained at 11.28 GHz, thereby satisfying the requirements for the TDMM. Overall, the low transmission of the meta-atom is mainly attributable to the power dissipation in the PIN diodes, which can be avoided by resorting to lower-loss components. Also, via further optimization of the structure design, or by using special distributions of electric and magnetic currents,[37] there is room for improvements to be explored in future designs.

In the first experiment, we implement the conditions of the example in Figure 2. Under a normally incident, *y*-polarized illumination, the transmitted field is received by a dual-polarized antenna, whose polarization channels are connected to two ports of a vector network analyzer (VNA). By comparing the signals at the two VNA ports (proportional to the complex-valued harmonic amplitudes A_k^x and A_k^y), the amplitude and phase differences can be obtained, and the polarization angle can be computed. By varying the duty cycle $R_x = t_1/T$ for the *x*-polarization, different polarization states at the central and harmonic frequencies can be synthesized, as shown in Figure 6e,f. Consistently with the theoretical results in Figure 2, when $p_2 = p_1$ the TDMM can rotate the impinging linear polarization by an arbitrary angle within the range [0°, 90°] at the central frequency, and can produce a linear polarization with an angle of –45° at the ±1st-order harmonic frequencies. On the other hand, for $p_1 = p_2 + 180°$, the rotation angle at the central frequency ranges within [–90°, 0°], and a linear polarization with an angle of 45° can be generated at the ±1st-order harmonic frequency.

Next, we move on to considering the scenario in Figure 4, by exploring the effects of the time delays t_x and t_y (in the *x*- and *y*-polarized channels, respectively) on the polarization states at the even-order harmonic frequencies. Figure 6g,h shows the measured phase differences at the ±2nd harmonic frequencies. By varying the time delay t_x (while maintaining $t_y = 0$), we observe opposite phase gradients at the ±2nd order harmonic frequencies for the *x*-polarization, with no effects on the harmonic phase for the *y*-polarization. Note that, in view of a different definition of the phase difference ($\angle A_k^y$-$\angle A_k^x$), the trends in Figure 6g are opposite to those in Figure 4c,e. Likewise, by varying the time delay t_y (with $t_x = 0$), only the harmonic phase for the *y*-polarization is affected (Figure 6h), consistent with the theoretical predictions in Figure 4d,e. Therefore, a broad tunability of the phase differences (between 0° and 360°) can be obtained by varying the time delays t_x and t_y. Note that, due to the strong polarization isolation in time, the phase-difference curves in Figure 6g,h exhibit an almost perfectly symmetrical behavior.

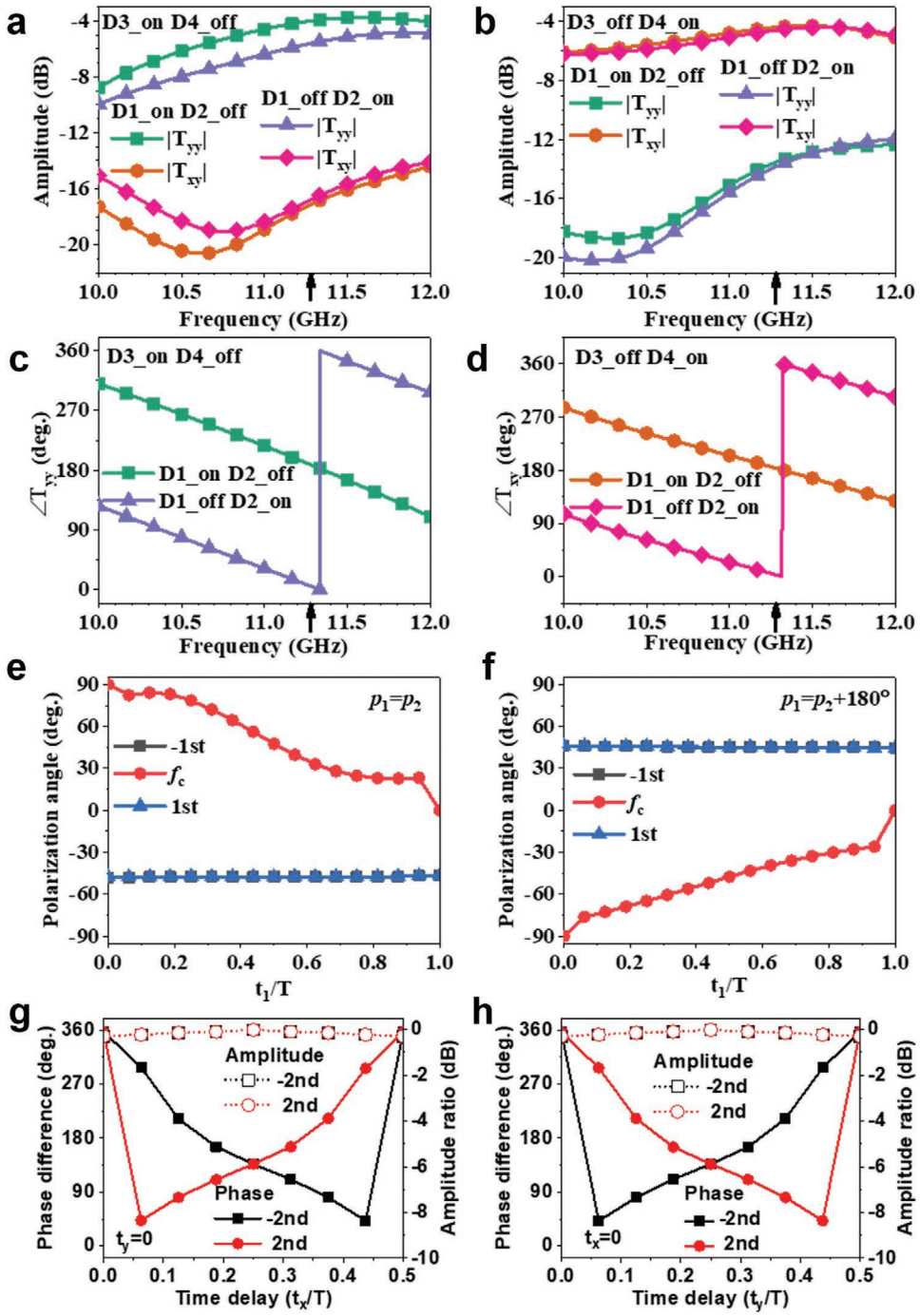

Figure 6. Experimental validation. a,c) Measured transmission amplitude and phase, respectively, of co-polarized component (PIN diodes: D3 on, D4 off), as a function of frequency, for different states of the PIN diodes D1 and D2. b,d) Same as above, but for cross-polarized component (PIN diodes: D3 off, D4 on). e,f) Measured polarization angle at central frequency and ±1st harmonic orders, as a function of duty cycle, for $p_1 = p_2 = 0°$ and $p_1 = 180°$, $p_2 = 0°$, respectively. g,h) Measured phase difference and amplitude ratio between the two polarizations at ±2nd harmonic orders, as a function of time delays t_x and t_y, respectively.

The above results demonstrate experimentally the independent phase control for two orthogonally polarized waves at the harmonic frequencies, which in turn enables the synthesis of desired polarizations states at selected harmonic orders, i.e., the simultaneous conversion of polarization and frequency.

3. Conclusion

In summary, we have put forward and demonstrated a mechanism for simultaneous conversion of polarization and frequency based on a TDMM platform relying on polarization switches. Different from conventional active/passive anisotropic

metasurfaces, the polarization states of the transmitted waves are intertwined in two temporal channels, and can be modulated periodically with suitably designed coding sequences. This enables the tailoring of the polarization states at the central and harmonic frequencies by acting on the duty cycle or the time delays in the polarization channels. We have fabricated and experimentally characterized an FPGA-controlled prototype, showing a good agreement with the theoretical predictions. These results significantly broaden the capabilities of space-time coding metasurfaces and set the stage for the development of a variety of new polarization-related devices.

Future developments include the expansion of the TDDM concept to realize simultaneous modulation of the amplitude, phase, frequency and polarization for incident waves, relying on advanced coding strategies. This would enable an efficient exploitation of the information resources in different domains, and shows great promises to enhance the channel capacity in future communication and radar systems.

Within this framework, some considerations are in order. Our proposed mechanism, via intertwined polarization channels in time, yields the superposition of two orthogonally polarized waves at the central or harmonic frequencies. However, the time-switching process of two orthogonally polarized waves brings inevitable limitations. Aiming at achieving polarization control at central frequency, the TDDM generates many different harmonic frequencies, which could be avoided by using an anisotropic element. Moreover, the harmonic efficiency of the polarization-control mechanism is mainly determined by the time-varying phase signals $\varphi_x(t)$ and $\varphi_y(t)$ in the two polarization channels. In the present study, due to the inherent limitations arising from 1-bit coding phase states, the harmonic efficiency at the selected harmonic frequencies is relatively low. However, by increasing the phase resolution (e.g., using higher-bit coding phase states), it is possible to realize simultaneous frequency and polarization conversion with high conversion efficiency by suitably designing the phase signals $\varphi_x(t)$ and $\varphi_y(t)$ (Figure S5, Supporting Information). We remark that although the proposed theory cannot be applied to directly control the polarization states at odd harmonic orders, TDDMs still hold some potentials in this respect, which will be explored in future studies (see also Figure S6, Supporting Information).

4. Experimental Section

Numerical Modeling: The response of the meta-atom in Figure 5 was modeled via full-wave numerical simulations based on the finite-volume integration in time domain, by relying on the commercial full-wave package CST Microwave Studio 2016 (https://www.3ds.com/products-services/simulia/products/cst-studio-suite/). Periodic boundary conditions and Floquet-type ports were utilized to account for mutual coupling effects among the neighboring elements.

Measurements: The schematics of the experimental setup for measuring the transmission coefficients and polarization angles at different harmonic frequencies are demonstrated in Figure S4 (Supporting Information). For measuring the transmission coefficient, two horn antennas were connected to a VNA (Keysight N5230C). One port of the VNA was connected to a feeding source, namely a standard-gain antenna (XB-HA75-20N) launching a quasi-plane wave with *y*-polarization. The other VNA port was connected to a dual-polarized wideband receiving antenna (LB-SJ-20180-SF), with two working modes for orthogonal linearly polarized waves. Via a comparison with a reference measurement in air, the metasurface transmission coefficient can be obtained. For measuring the polarization angle at different harmonic frequencies, the *y*-polarized feeding source was connected to a microwave signal generator (Keysight E8257D), while the two polarization channels of the receiving antenna were connected to the two VNA ports. The VNA thus worked as a two-port receiver to compare the orthogonally polarized signals received signals, and a phase-locked loop was used to ensure the synchronization with the signal generator. From the measurements of the complex-valued harmonic amplitudes A_k^x and A_k^y, the polarization angle was finally obtained. To provide the required dynamic biasing voltages for the metasurface, an FPGA hardware control board (Artix-7) was utilized. Two channel signals were used to control the PIN diodes D3 and D4 for the amplitude waveforms, and D1 and D2 for the phase waveforms, respectively. A modulation frequency f_0 = 1 kHz was assumed. The detection (sampling) time affected the targeted polarization state. In order to observe stable harmonic waves, such time should be much longer than the modulation period *T*.

Supporting Information

Supporting Information is available from the Wiley Online Library or from the author.

Acknowledgements

J.Y. and J.C.K. contributed equally to this work. This work was supported in part by the National Key Research and Development Program of China (2017YFA0700201, 2017YFA0700202, 2017YFA0700203, and 2018YFA0701904), in part by the National Natural Science Foundation of China (Grant Nos. 61631007, 61571117, 61501112, 61501117, 61522106, 61731010, 61735010, 61722106, 61701107, and 61701108), in part by the 111 Project (Grant No. 111-2-05), in part by the Postgraduate Research & Practice Innovation Program of Jiangsu Province (KYCX18_0097), and in part by the Scientific Research Foundation of the Graduate School of Southeast University (YBPY1858). Open Access Funding provided by Universita degli Studi del Sannio within the CRUI-CARE Agreement.

Conflict of Interest

The authors declare no conflict of interest.

Data Availability Statement

Research data are not shared.

Keywords

frequency conversion, metasurfaces, polarization conversion, time-modulated polarization

Received: May 25, 2021
Revised: July 23, 2021
Published online:

[1] E. Ongareau, A. Roussaud, E. Marouby, J. R. Levrel, *Microw. Opt. Technol. Lett.* **1995**, *8*, 316.
[2] Y. Liu, K. Li, Y. Jia, Y. Hao, S. Gong, Y. J. Guo, *IEEE Trans. Antennas Propag.* **2015**, *64*, 326.

[3] Y. Jia, Y. Liu, Y. J. Guo, K. Li, S. Gong, *IEEE Trans. Antennas Propag.* **2016**, *64*, 179.
[4] M. Ikram, N. Nguyen-Trong, A. Abbosh, *IEEE Trans. Antennas Propag.* **2019**, *68*, 4991.
[5] A. Arbabi, Y. Horie, M. Bagheri, A. Faraon, *Nat. Nanotechnol.* **2015**, *10*, 937.
[6] Q. Bao, H. Zhang, B. Wang, Z. Ni, C. H. Y. X. Lim, Y. Wang, D. Y. Tang, K. P. Loh, *Nat. Photonics* **2011**, *5*, 411.
[7] A. E. Minovich, A. E. Miroshnichenko, A. Y. Bykov, T. V. Murzina, D. N. Neshev, Y. S. Kivshar, *Laser Photonics Rev.* **2015**, *9*, 195.
[8] S. Zhang, J. Zhou, Y.-S. Park, J. Rho, R. Singh, S. Nam, A. K. Azad, H.-T. Chen, X. Yin, A. J. Taylor, X. Zhang, *Nat. Commun.* **2012**, *3*, 942.
[9] L. Cong, N. Xu, W. Zhang, R. Singh, *Adv. Opt. Mater.* **2015**, *3*, 1176.
[10] R. H. Phillion, M. Okoniewski, *IEEE Trans. Antennas Propag.* **2011**, *59*, 1217.
[11] D. Lin, P. Fan, E. Hasman, M. Brongersma, *Science* **2014**, *345*, 298.
[12] Y. Yang, W. Wang, P. Moitra, I. I. Kravchenko, D. P. Briggs, J. Valentine, *Nano Lett.* **2014**, *14*, 1394.
[13] Y. Hu, X. Wang, X. Luo, X. Ou, L. Li, Y. Chen, P. Yang, S. Wang, H. Duan, *Nanophotonics* **2020**, *9*, 3755.
[14] K. Chen, N. Zhang, G. Ding, J. Zhao, T. Jiang, Y. Feng, *Adv. Mater. Technol.* **2020**, *5*, 1900930.
[15] J. Yang, C. Zhang, H. F. Ma, J. Zhao, J. Y. Dai, W. Yuan, L. X. Yang, Q. Cheng, T. J. Cui, *Appl. Phys. Lett.* **2018**, *112*, 203501.
[16] J. Yang, C. Zhang, H. Ma, W. Yuan, L. Yang, J. Ke, M. Chen, A. Mahmoud, Q. Cheng, T. J. Cui, *Opt. Express* **2018**, *26*, 31664.
[17] N. K. Grady, J. E. Heyes, D. R. Chowdhury, Y. Zeng, M. T. Reiten, A. K. Azad, A. J. Taylor, D. A. R. Dalvit, H.-T. Chen, *Science* **2013**, *340*, 1304.
[18] S. Liu, T. J. Cui, Q. Xu, D. Bao, L. Du, X. Wan, W. X. Tang, C. Ouyang, X. Y. Zhou, H. Yuan, H. F. Ma, W. X. Jiang, J. Han, W. Zhang, Q. Cheng, *Light: Sci. Appl.* **2016**, *5*, 16076.
[19] J. P. B. Mueller, N. A. Rubin, R. C. Devlin, B. Groever, F. Capasso, *Phys. Rev. Lett.* **2017**, *118*, 113901.
[20] X. Ding, F. Monticone, K. Zhang, L. Zhang, D. Gao, S. N. Burokur, A. de Lustrac, Q. Wu, C.-W. Qiu, A. Alù, *Adv. Mater.* **2015**, *27*, 1195.
[21] D. Wen, F. Yue, G. Li, G. Zheng, K. Chan, S. Chen, M. Chen, K. F. Li, P. W. H. Wong, K. W. Cheah, E. Y. B. Pun, S. Zhang, X. Chen, *Nat. Commun.* **2015**, *6*, 8241.
[22] M. Jia, Z. Wang, H. Li, X. Wang, W. Luo, S. Sun, Y. Zhang, Q. He, L. Zhou, *Light: Sci. Appl.* **2019**, *8*, 16.
[23] T. J. Cui, M. Q. Qi, X. Wan, J. Zhao, Q. Cheng, *Light: Sci. Appl.* **2014**, *3*, 218.
[24] J. Lončar, A. Grbic, S. Hrabar, *Phys. Rev. B* **2019**, *100*, 075131.
[25] A. Zhang, R. Yang, *Phys. Rev. B* **2019**, *100*, 245421.
[26] D. Floess, J. Y. Chin, A. Kawatani, D. Dregely, H.-U. Habermeier, T. Weiss, H. Giessen, *Light: Sci. Appl.* **2015**, *4*, 284.
[27] L. H. Nicholls, F. J. Rodríguez-Fortuño, M. E. Nasir, R. M. Córdova-Castro, N. Olivier, G. A. Wurtz, A. V. Zayats, *Nat. Photonics* **2017**, *11*, 628.
[28] J. Zhao, X. Yang, J. Y. Dai, Q. Cheng, X. Li, N. H. Qi, J. C. Ke, G. D. Bai, S. Liu, S. Jin, A. Alù, T. J. Cui, *Natl. Sci. Rev.* **2019**, *6*, 231.
[29] J. Y. Dai, J. Zhao, Q. Cheng, T. J. Cui, *Light: Sci. Appl.* **2018**, *7*, 90.
[30] L. Zhang, X. Q. Chen, S. Liu, Q. Zhang, J. Zhao, J. Y. Dai, G. D. Bai, X. Wan, Q. Cheng, G. Castaldi, V. Galdi, T. J. Cui, *Nat. Commun.* **2018**, *9*, 4334.
[31] L. Zhang, X. Q. Chen, R. W. Shao, J. Y. Dai, Q. Cheng, G. Castaldi, V. Galdi, T. J. Cui, *Adv. Mater.* **2019**, *31*, 1904069.
[32] J. C. Ke, J. Y. Dai, M. Z. Chen, L. Wang, C. Zhang, W. Tang, J. Yang, W. L. Xin, L. Y. Lu, Q. Cheng, S. Jin, T. J. Cui, *Small Struct.* **2021**, *2*, 2000060.
[33] G. Castaldi, L. Zhang, M. Moccia, A. Y. Hathaway, W. X. Tang, T. J. Cui, V. Galdi, *Adv. Funct. Mater.* **2021**, *31*, 2007620.
[34] L. Zhang, J. Y. Dai, M. Moccia, G. Castaldi, T. J. Cui, V. Galdi, *EPJ Appl. Metamater.* **2020**, *7*, 7.
[35] J. Yang, J. C. Ke, M. Chen, M. Z. Chen, J. Y. Dai, J. F. Chen, R. Yang, J. W. Wu, Q. Cheng, T. J. Cui, *Photonics Res.* **2021**, *9*, 344.
[36] W. Pan, C. Huang, X. Ma, B. Jiang, X. Luo, *IEEE Antennas Wirel. Propag. Lett.* **2015**, *14*, 167.
[37] K. Chen, Y. Feng, F. Monticone, J. Zhao, B. Zhu, T. Jiang, L. Zhang, Y. Kim, X. Ding, S. Zhang, A. Alù, C. W. Qiu, *Adv. Mater.* **2017**, *29*, 1606422.